

Article

A Y-Type Air-Cooled Battery Thermal Management System with a Short Airflow Path for Temperature Uniformity

Xiangyang Li ¹, Jing Liu ^{1,*} and Xiaomin Li ²

¹ School of Information Engineering and Internet of Things, Huzhou Vocational & Technical College, Huzhou 313000, China; 2021046@huvtc.edu.cn

² School of Information Engineering, Henan Institute of Science and Technology, Xinxiang 453003, China; 213104000049@njjust.edu.cn

* Correspondence: 2021044@huvtc.edu.cn; Tel.: +86-188-6786-1965

Abstract: A Y-type air-cooled structure has been proposed to improve the heat dissipation efficiency and temperature uniformity of battery thermal management systems (BTMSs) by reducing the flow path of air. By combining computational fluid dynamics (CFD) methods, the influence of the depths of the distribution and convergence plenums on the airflow velocity through battery cells was analyzed to improve heat dissipation efficiency. Adjusting the width of the first and ninth cooling channels can change the air velocity of these two channels, thereby improving the temperature uniformity of the BTMS. Further discussion was conducted regarding the influences of inlet and outlet depths. When the inlet width and outlet width were 20 mm, the maximum temperature and maximum temperature difference of the Y-type BTMS were 39.84 °C and 0.066 °C at a discharge rate of 2.5 °C, respectively; these temperatures were 1.537 °C (3.68%) and 0.059 °C (47.2%) lower than those of the T-type model. Meanwhile, the energy consumption of the sample also decreased by 13.1%. The results indicate that the heat dissipation performance of the proposed Y-type BTMS was improved, achieving excellent temperature uniformity, and the energy consumption was also reduced.

Keywords: lithium-ion battery pack; battery thermal management system; air-cooled; Y-type structure; temperature uniformity



Citation: Li, X.; Liu, J.; Li, X. A Y-Type Air-Cooled Battery Thermal Management System with a Short Airflow Path for Temperature Uniformity. *Batteries* **2024**, *10*, 302. <https://doi.org/10.3390/batteries10090302>

Academic Editor: Vilas Pol

Received: 5 July 2024

Revised: 12 August 2024

Accepted: 26 August 2024

Published: 27 August 2024



Copyright: © 2024 by the authors. Licensee MDPI, Basel, Switzerland. This article is an open access article distributed under the terms and conditions of the Creative Commons Attribution (CC BY) license (<https://creativecommons.org/licenses/by/4.0/>).

1. Introduction

Energy is one of the most important issues for politicians and government officials in various countries. Therefore, researchers have attached great importance to this discussion [1–3]. Fossil fuel resources will eventually be depleted; therefore, it is necessary to search for new available energy sources. This has led to many countries investing more in electric vehicles. The main component of electric vehicles is the battery [4,5]. A lithium-ion battery pack composed of hundreds or thousands of battery units integrated in series and in parallel inevitably accumulates a large amount of heat during discharge. If heat dissipation is not carried out, heat loss problems can easily result, affecting the working performance and safety of the battery.

The cooling systems in electric and hybrid vehicles can be active or passive cooling systems; air, liquid or phase-change materials cooling; single cooling systems or combined cooling and heating systems and direct or indirect cooling systems. A BTMS based on forced air cooling technology is the simplest method to solve the problem of internal heating in battery packs and provides a feasible solution when the internal design space of electric vehicles is tight. The air-cooled BTMS is also the foundation of other cooling technologies, and other cooling technologies usually require air cooling technology to be used in conjunction. The application limitations of air-cooled BTMSs are becoming increasingly apparent. However, in terms of actual usage effects, it is still suitable for some pure electric/hybrid electric vehicles with moderate battery energy density or equipped with lithium iron phosphate batteries. For this type of electric vehicle, due to the fact that

the heat generated by the battery does not rapidly increase, a forced air cooling BTMS is sufficient to maintain the thermal balance of the system. Many researchers have proposed different battery cooling solutions over recent years [6,7]. The effects of quantity [8–10] and location [11,12] of the inlets and outlets on heat dissipation performance have been studied. Hong et al. [10] improved the cooling performance of Z-type air-cooled BTMS by adding a secondary outlet. Peng et al. [13] analyzed the influence of the position and height of the inlet and outlet on the cooling performance of U-type battery packs. Zhang et al. [14] designed an air-cooled T-type BTMS. Compared to others, T-type BTMS has better cooling performance and energy consumption.

The key to designing the structure of an air-cooled BTMS is to carefully consider the impact of the flow and distribution of cooling air on the cooling performance of the battery pack. As shown in Figure 1, the Z-type and U-type BTMS are in series. The T-type BTMS is a parallel type, and its cooling performance is significantly better than that of the Z-type and U-type BTMSs at the same inlet flow rate. However, the T-type BTMS also has similar defects as Z-type and U-type BTMS, especially the long airflow path makes it difficult for the cooling air to continue dissipating heat for the battery when flowing near the outlet due to its high temperature. Taking inspiration from this, we absorb and improves the T-type structure, proposes a Y-type BTMS with a symmetrical flow field, retains the parallel structure, optimizes the layout of the inlet and outlet, shortens the airflow path and is expected to enable the BTMS to achieve better heat dissipation performance and better thermal uniformity. This paper proposes a Y-type air-cooled BTMS for a 1×8 arrangement in a square lithium-ion battery pack, providing a feasible cooling solution for electric/hybrid vehicles equipped with iron phosphate batteries in compact vehicle design spaces or requiring light weight.

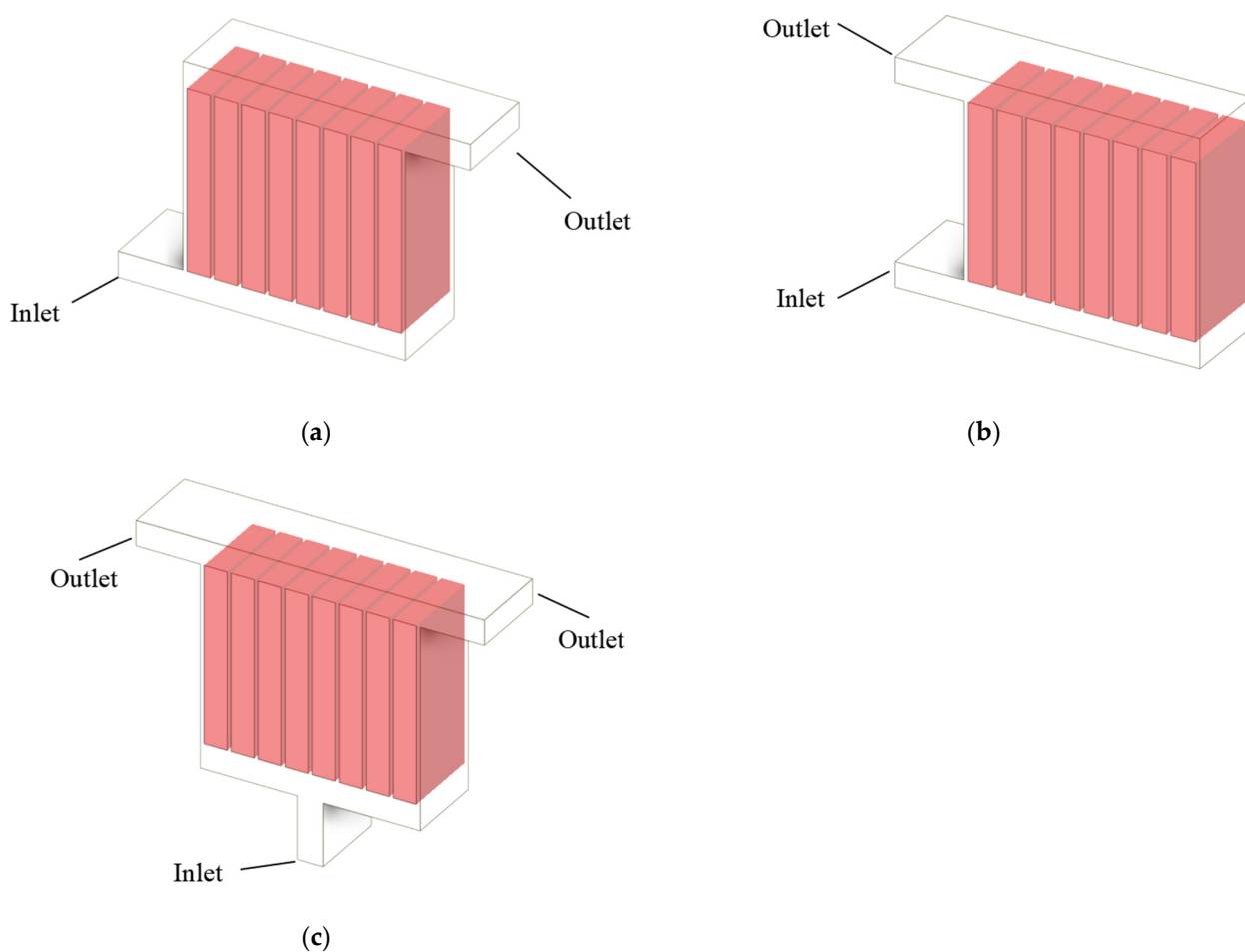


Figure 1. Structural design of BTMSs. (a) Z-type; (b) U-type; (c) T-type.

2. Model and Methodology

2.1. Model Description

The Y-type air-cooled BTMS shown in Figure 2 consists of 8 prismatic cells arranged in series and 9 cooling channels. Considering the volume limitation of automotive BTMSs, the system includes an external battery box similar to a Y-type skeleton and 8 square lithium-ion batteries arranged parallel to the x -axis direction. The batteries are tightly connected to the wall on both sides along the length direction. The size of the battery cell is $65 \times 18 \times 140$ mm (length \times width \times height). The inlet air rate is 5.2×10^{-3} m³/s, and the inlet is located in the middle of the side of the box. Two outlets are symmetrically arranged on opposite sides of the box. The cooling air spreads out in a distribution plenum and flows into 9 cooling channels for heat exchange with continuously discharging batteries. Finally, it converges through a convergence plenum and flows out from the outlet areas on both sides.

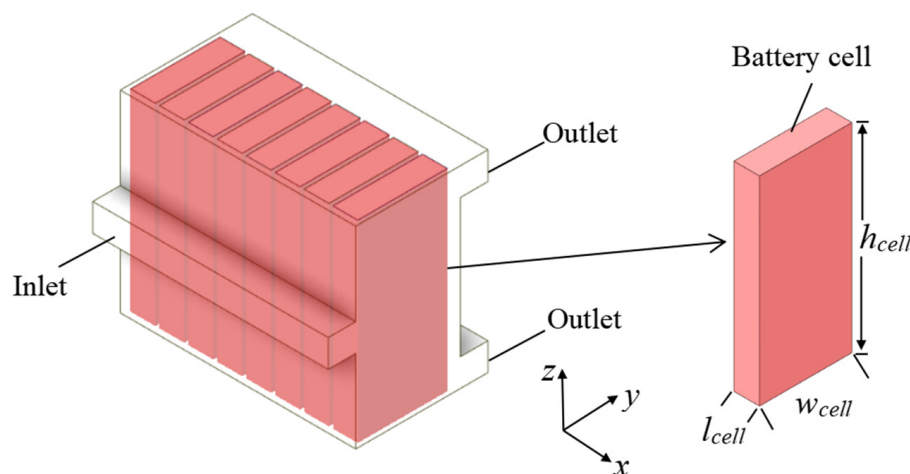


Figure 2. Three-dimensional model of Y-type air-cooled BTMS and battery cell.

As is well known, due to the heat-dissipating effect of airflow, the temperature between the inlet and outlet of a BTMS varies greatly. The inlet air temperature is lower, while the outlet air temperature is higher, forming a large temperature gradient at both ends of the battery. In the Y-type BTMS, the airflow from the distribution plenum to the convergence plenum is shortened along the length direction of the battery, which reduces the time for the battery to heat the air and lowers the temperature of the battery near the outlet, resulting in better cooling performance of the system. For the Y-type BTMS, because there are two outlets, the cooling channel is divided into two symmetrical parts along the height direction of the battery during operation. Each part is allocated half of the cooling airflow, which may cause the temperature of the battery to increase near the inlet, thereby reducing the temperature gradient. It can be expected that the Y-type BTMS will achieve better uniformity.

This study used the air parameters shown in Table 1 and the battery cell parameters shown in Table 2 in the numerical calculations for the Y-type BTMS.

Table 1. Physical properties of air.

Properties	Unit	Air
Density	kg·m ⁻³	1.165
Specific Heat Capacity C _P	J·kg ⁻¹ ·K ⁻¹	1005
Thermal Conductivity	W·m ⁻¹ ·K ⁻¹	0.0267
Viscosity	kg·m ⁻¹ ·s ⁻¹	1.86×10^{-5}

Table 2. Physical properties of a battery cell when the discharge rate is 2.5 C.

Properties	Unit	Cell
Density	$\text{kg}\cdot\text{m}^{-3}$	2136.8
Specific Heat Capacity C_p	$\text{J}\cdot\text{kg}^{-1}\cdot\text{K}^{-1}$	1633
Thermal Conductivity	$\text{W}\cdot\text{m}^{-1}\cdot\text{K}^{-1}$	$\lambda_z = 1, \lambda_x = \lambda_y = 29$
Heat Generation Rate	$\text{W}\cdot\text{m}^{-3}$	60,439.56

2.2. Numerical Model

2.2.1. Control Equation

CFD is a common computer numerical simulation method. The current mainstream CFD calculation methods are based on commercial software and can be simplified into three main processes: modeling, numerical computation and result output. Compared with experiments, they have the advantages of low cost and high reliability, making them an effective means to solve thermal engineering problems.

In this study, the Y-type lithium-ion battery pack was modeled using the CFD method to calculate the velocity and temperature fields of BTMS. In order to simplify the calculation process and take into account the complexity of air flow and battery heating in BTMS, several assumptions were made: (1) that the Mach number Ma of the cooling air is much smaller than 0.3 due to its compressibility; (2) that the buoyancy effect of the air is negligible; (3) that the battery case is insulated and has no relative slip with the air; (4) that, during the heating process, the influence of temperature on the physical properties of air and battery materials can be ignored; (5) that the ambient temperature will not change over time after being set; (6) that lithium ion batteries are uniform solids with constant, anisotropic thermal conductivity and constant specific heat capacity; and (7) that the thermal deformation of the heat dissipation system is negligible.

The flow process should follow the laws of mass, momentum, energy and turbulent transport equations [15].

The continuity equation is as follows:

$$\frac{\partial u_i}{\partial x_i} = 0 \quad (1)$$

where u_i is the i th Reynolds average velocity component.

The momentum conservation equation is as follows:

$$\rho_a u_j \frac{\partial u_i}{\partial x_j} = -\frac{\partial p_a}{\partial x_i} + \frac{\partial}{\partial x_j} [(\mu + \mu_t) \frac{\partial u_i}{\partial x_j}] \quad (2)$$

where ρ_a and p_a are the density and static pressure of air, while μ and μ_t are the molecular dynamic viscosity coefficient and turbulent dynamic viscosity coefficient, respectively.

The energy conservation equation is as follows:

$$\frac{\partial(\rho_a C_a T_a)}{\partial t} + \nabla \cdot (\rho_a C_a \vec{v} T_a) = \nabla \cdot (k_a \nabla T_a) \quad (3)$$

where C_a , k_a , \vec{v} and T_a are the specific heat, thermal conduction coefficient, velocity and temperature of air, respectively.

Before determining the control equation, it was necessary to determine the flow state of the air in the battery pack. The system's Reynolds number was calculated as 3409 by Formulas (4) and (5). In this study, the flow state of cooling air inside the system was turbulent.

$$\text{Re} = \frac{\rho_a u D}{\mu} \quad (4)$$

$$D = \frac{2H_{in}L_{in}}{H_{in} + L_{in}} \quad (5)$$

where Re is the Reynolds number; the value of inlet wind speed u is 1.52 m/s; D is the feature length and the inlet height H_{in} and length L_{in} are 20 mm and 171 mm, respectively.

Based on the standard $k - \varepsilon$ turbulence model, the air flow rate was calculated using the NS equations. In the $k - \varepsilon$ model, k represents turbulent kinetic energy and ε represents turbulent dissipation rate. The equations are shown below.

The turbulent kinetic energy equation is as follows:

$$\frac{\partial}{\partial t}(\rho_a k) + \frac{\partial}{\partial x_j}(\rho_a k u_j) = \frac{\partial}{\partial x_j} \left(\left(\mu + \frac{\mu_t}{\alpha_k} \right) \frac{\partial k}{\partial x_j} \right) + G_k + G_b - \rho_a \varepsilon - Y_M + S_k \quad (6)$$

The turbulent kinetic energy dissipation equation is as follows:

$$\begin{aligned} \frac{\partial}{\partial t}(\rho_a \varepsilon) + \frac{\partial}{\partial x_j}(\rho_a \varepsilon u_j) = \\ \frac{\partial}{\partial x_j} \left(\left(\mu + \frac{\mu_t}{\alpha_\varepsilon} \right) \frac{\partial \varepsilon}{\partial x_j} \right) + C_{1\varepsilon} \frac{\varepsilon}{k} (G_k + C_{3\varepsilon} G_b) - \rho C_{2\varepsilon} \frac{\varepsilon^2}{k} + S_\varepsilon \end{aligned} \quad (7)$$

where u_j is the j th component of the velocity vector; G_k is the turbulent kinetic energy generated by the smooth velocity gradient; G_b is the turbulent energy generated by the buoyancy factor; Y_M is the influence factor of turbulent pulsation on the total dissipation rate; $C_{1\varepsilon}$, $C_{2\varepsilon}$ and $C_{3\varepsilon}$ are empirical constants; α_k and α_ε are Prandtl numbers corresponding to the turbulent kinetic energy and turbulent kinetic energy dissipation rate and S_k and S_ε are the source terms of k and ε , respectively.

In addition, the heat generated within the battery area of the battery pack includes internal waste heat and heat carried away by air, and its energy conservation equation can be expressed as follows [16]:

$$\rho_b C_{pb} \frac{\partial T}{\partial t} = \nabla \cdot (k_b \nabla T) + \dot{Q} \quad (8)$$

where ρ_b , C_{pb} , k_b and \dot{Q} are the density, specific heat capacity, thermal conductivity and heat generation of the battery, respectively.

2.2.2. Mesh Generation and Evaluation

For the proposed Y-type BTMS, the geometry model of the battery pack module was constructed using Design Modeler software (Ansys DesignModeler 2022 R1) and imported into Fluent Meshing without adding local dimensions, and then mesh partitioning and repair were performed. In mesh partitioning mode, the Fluent function can handle meshes of almost infinite size and complexity.

The volume meshes can be generated from boundary meshes to ensure a good starting point for generating volume meshes. Various properties of the computational surface mesh should be specified and adjusted until the surface mesh accurately captures the topology of the imported CAD geometry. There should be no gaps or fragments, and the surface mesh of key areas should be refined to ensure that important physical behaviors in CFD analysis can be captured. For the elements of the surface grid, a minimum size of 0.0001 m and a maximum size of 0.003 m were specified. The edge length of each subsequent element layer was increased by 1.2. The type of size function applied to surface meshes was selected based on curvature and proximity. Given a specific geometric curvature, the maximum allowable angle for an element edge to cross was specified as 18. The minimum number of layers generated in the gap was 1. We set the refinement based on proximity of edges, while considering the proximity from edge to edge. The types of imported geometry consist of solid models and fluid models. The types of inlet and outlet boundaries were specified as walls.

Five boundary layers were added to the solid area along the walls of the model. The type of offset was selected as smooth transition, which determines how to generate the mesh elements closest to the boundary. For the smooth transition migration method, adjacent elements grow at a rate of 0.272, while for the boundary layer, the growth rate is 1.2.

For the entire volume within the geometry, the meshes were composed of polyhedral elements. In addition to the fluid region, the solid region was also meshed. Element size control, such as growth rate and maximum cell length, was evaluated globally. The number of additional layers required for rapid transition between finer elements in the boundary grid and coarser elements in the initial Cartesian grid is 2. The number of layers controlling the gap between the hexahedral core and the geometric shape is 1. For the volume-filling type of polyhedral core, the minimum unit length is 0.0001 and the maximum unit length is 0.0032. In order to perform volume mesh partitioning faster and more effectively, parallel settings are used to generate computational meshes.

After calculating the grid generation, orthogonal quality was used to evaluate the grid. In general, the minimum orthogonal quality of the mesh is required to be greater than 0.2. If the mesh quality is higher than 0.2 but relatively low, a highly skewed mesh can be improved by moving the nodes of the elements. The node movement process used to improve grid quality is automated, and the user can specify quality improvements based on specified quality measures. In this study, the mesh quality requirement needed to be higher than 0.3. Figure 3 shows a 3D mesh model of the battery pack casing, where the cutting plane is inserted along the plane normal to the X-axis, in which case the minimum orthogonal mass occurred in the air, i.e., the fluid region, with a value of 0.52575382, while the unit portion, i.e., the solid region, had a larger orthogonal mass.

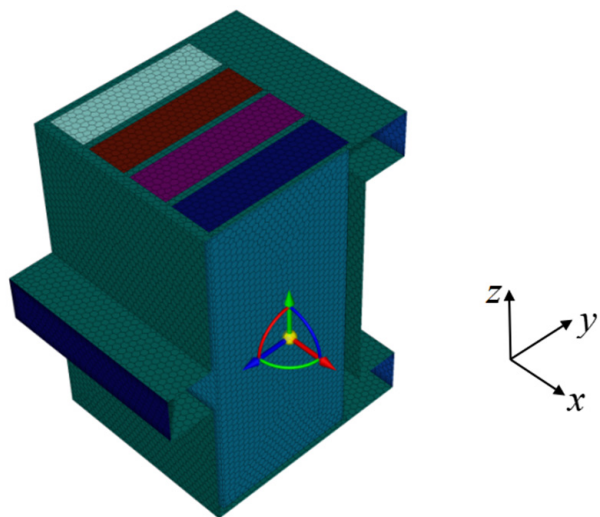


Figure 3. Half of the 3D mesh model of the battery pack cut in cross-section normal to the X-axis.

2.3. Calculation Process

2.3.1. Boundary Conditions

Using the software FLUENT (Fluent 2022 R1) to solve the above control equations, in order to achieve accurate solutions, the following boundary conditions were set for the BTMS. Unless otherwise specified, the initial temperature of all zones was 25 °C, and the air pressure was standard atmospheric pressure. The air inlet was the velocity inlet, and the air outlet was the standard atmospheric pressure outlet. The battery box wall was an insulated anti-slip wall, and an enhanced wall function was used when near-wall treatment was required. The pressure–velocity coupling scheme used the SIMPLE algorithm, and the mass flux type used distance-based Rhie–Chow. The gradient calculation method for controlling the spatial discretization of the convection term in the solution equation was set based on the least squares element. The discretization scheme of the pressure equation

was second-order, while the discretization of the momentum and energy equations was second-order upwind. The solution of energy was considered to converge with a residual value set to 1×10^{-7} .

2.3.2. CFD Model Validation

The numerical simulation model and CFD method for battery packs were to be used for subsequent optimization research, and their reliability is crucial for the optimization analysis of BTMS.

Zhang et al. [14] conducted experimental research on the T-type air-cooled BTMS model and performed simulation and experimental analysis; more details can be found in reference [14]. This paper simulated the forced air cooling of T-type BTMS battery pack based on the above methods and compares the simulation results with those in reference [14]. The temperature simulated here corresponded to the same time (end of discharge) and operating conditions (discharge rate, air flow rate, air inlet temperature, etc.) as the literature. As shown in Figure 4, the maximum temperature of each single cell in the battery pack (T_c) at the end of discharge at 2.5 °C using this method was compared with the highest temperature in reference [14], and its relative error was calculated. When the inlet velocity was 3 m/s, the maximum temperature difference between cell 4 in this method and cell 4 in reference [14] was only 0.186 °C, with a corresponding maximum relative error of 0.96%. This indicates that the proposed method is effective and feasible.

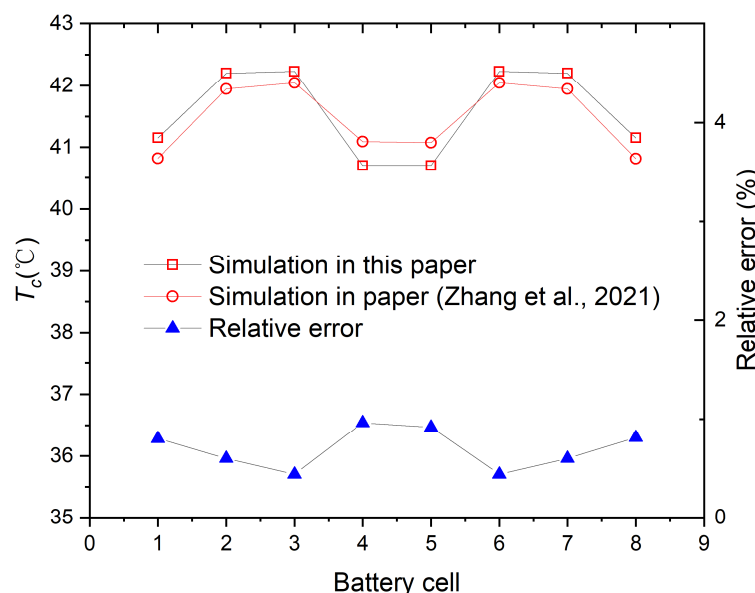


Figure 4. Comparison between the simulation results of a T-type air-cooled BTMS battery pack in this paper and the results given in reference [14]. Copyright (2024), with permission from Elsevier.

3. Results and Discussion

3.1. Distribution Plenum and Convergence Plenum

3.1.1. Distribution Plenum and Convergence Plenum with Same Depth

For the convenience of quantitative evaluation, the thermal characteristics of the BTMS were evaluated by using the maximum temperature (T_{\max}) of the battery pack and the maximum temperature difference (ΔT_{\max}) between each individual cell in the battery pack. It can be clearly seen from the Y-type BTMS structure in Figure 5 that the sizes of the distribution plenum and convergence plenum had an impact on the air flow velocity, thereby affecting the thermal characteristics of the system.

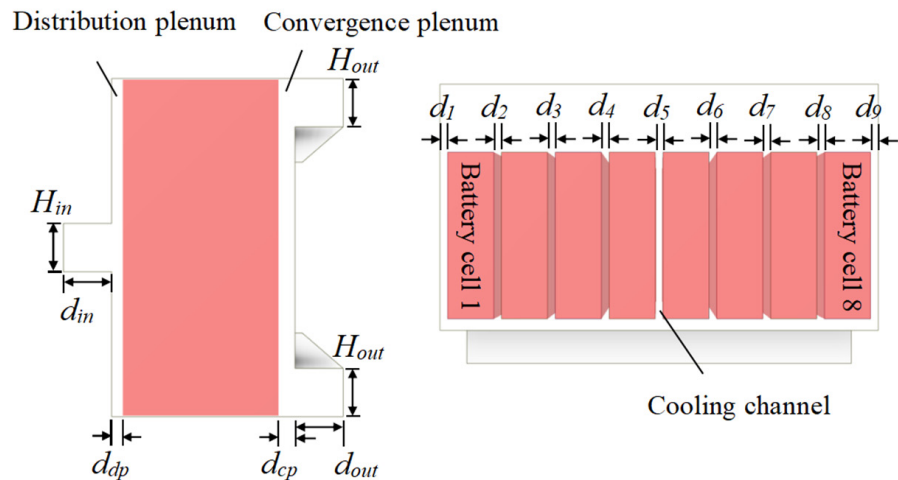


Figure 5. Right and top views of a Y-type air-cooled BTMS.

As shown in Figure 5, considering that the dimensions of d_{dp} and d_{cp} were equal, their values ranged from 2.5 mm to 20 mm. The inlet width d_{in} , outlet width d_{out} , inlet height H_{in} and outlet height H_{out} were all 20 mm, and the widths (d_1-d_9) of all cooling channels were set to 3 mm. The battery was set to discharge at 2.5 °C, with an air flow velocity of 1.52 m/s, corresponding to a total flow rate of $5.2 \times 10^{-3} \text{ m}^3 \cdot \text{s}^{-1}$, which is consistent with reference [14]. Figure 6 shows the effect of d_{dp} and d_{cp} on T_c , and the heat dissipation performance of BTMS was similar when the d_{dp} values were 5 mm, 5.5 mm and 6 mm. The performance was optimal when d_{dp} is 5.5 mm, with T_{\max} of 40.486 °C and ΔT_{\max} of 0.501 °C. Compared with the optimal T_{\max} after adding turbulence plates in reference [5], T_{\max} was decreased by 0.876 °C (2.1%).

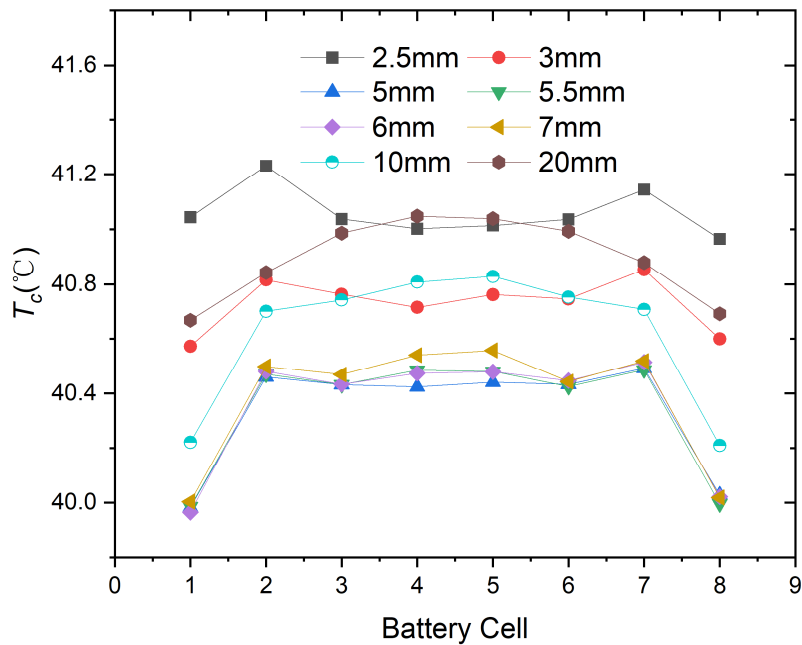


Figure 6. The impact of d_{dp} and d_{cp} on T_c , where d_{dp} and d_{cp} are equal and range from 2.5 mm to 20 mm.

Heat dissipation performance is closely related to air flow velocity. T_{\max} and the maximum flow velocity (V_{\max}) at the X-axis centerline position are shown in Figure 7. As d_{dp} increased from 2.5 mm to 20 mm, V_{\max} gradually decreased from 5.467 m/s to 2.875 m/s. Generally speaking, the smaller the flow velocity, the worse the heat dissipation

performance, while the larger the flow velocity, the better the heat dissipation performance. As d_{dp} increased from 5.5 mm to 20 mm, T_{max} gradually increased from 40.486 °C to 41.048 °C, which conforms to the general rule of the relationship between flow velocity and heat dissipation performance. However, when d_{dp} increased from 2.5 mm to 5.5 mm, T_{max} gradually decreased from 41.231 °C to 40.486 °C, which does not conform to the general rule of the relationship between flow velocity and heat dissipation performance.

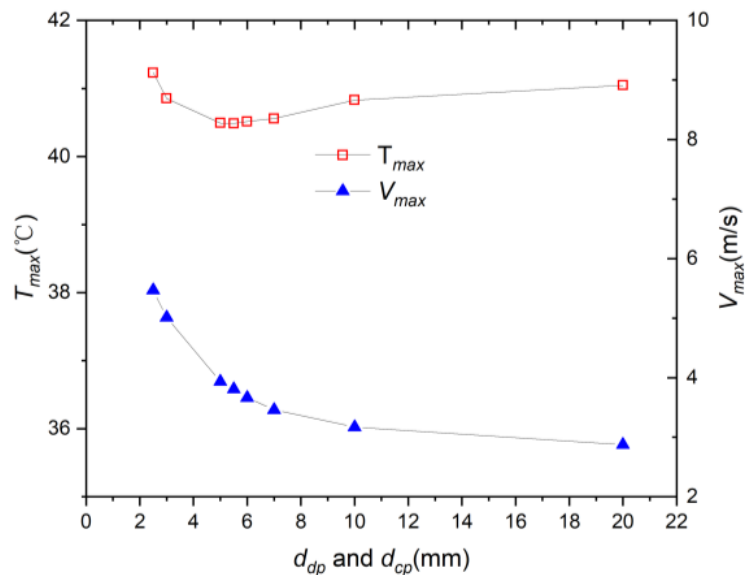


Figure 7. T_{max} of the system and V_{max} at the cross-sectional position of the system in the X-axis.

Figure 8 shows the velocity cloud map located at the X-axis cross-section (in channel 5). When d_{dp} was 2.5 mm and 3 mm, eddy currents were observed in Figure 8a,b, which may make it difficult for air to enter the top of distribution plenum and affect the stability of fluid flow. That is to say, when d_{dp} is small, the heat dissipation performance of the system is affected not only by the flow velocity but also by eddy currents. This can explain why, when d_{dp} increased from 2.5 mm to 5.5 mm, the flow velocity decreased while the heat dissipation performance of the system still improved. When drawing a fluid velocity cloud map and calculating V_{max} , the cross-section taken was the projection plane of the battery unit in the YZ plane, where the Y-axis and Z-axis dimensions of the fluid region were equal to the Y-axis and Z-axis dimensions of the battery cells, respectively. This could provide more accurate results.

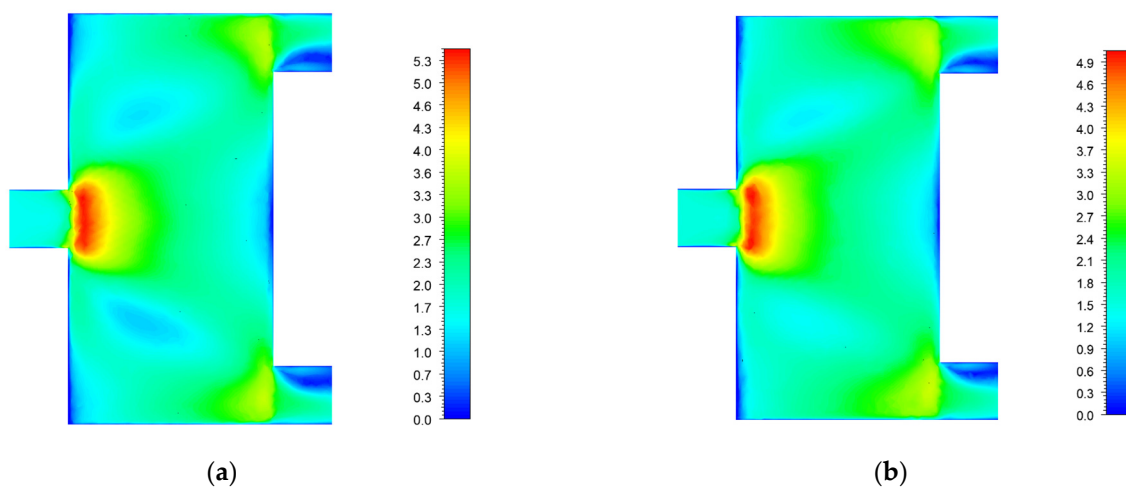


Figure 8. Cont.

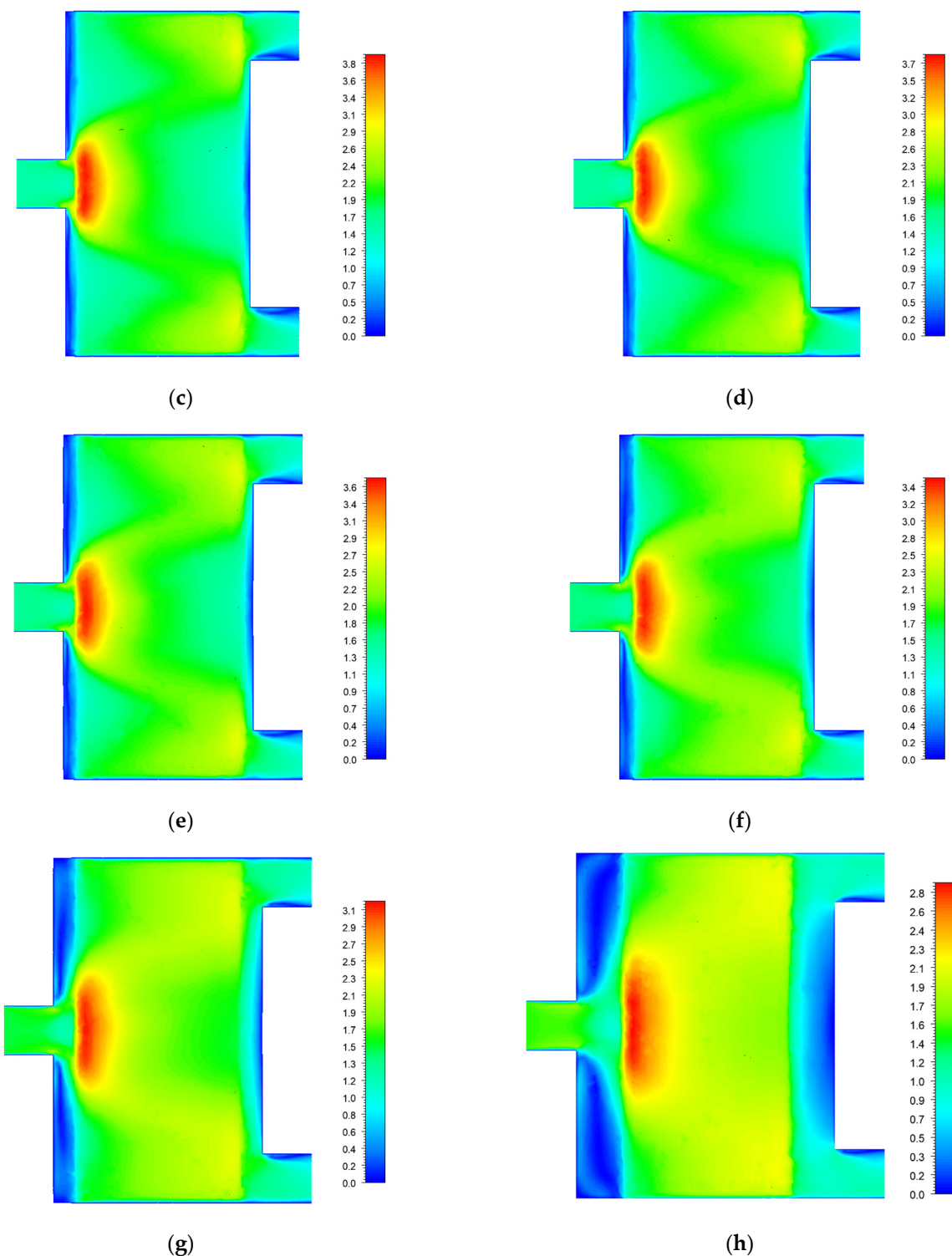


Figure 8. The velocity cloud map located in the X-axis cross-section, where d_{dp} and d_{cp} are equal. (a) $d_{dp} = 2.5$ mm; (b) $d_{dp} = 3$ mm; (c) $d_{dp} = 5$ mm; (d) $d_{dp} = 5.5$ mm; (e) $d_{dp} = 6$ mm; (f) $d_{dp} = 7$ mm; (g) $d_{dp} = 10$ mm; (h) $d_{dp} = 20$ mm.

3.1.2. Distribution Plenum and Convergence Plenum with Different Depths

As shown in Figure 6, when both d_{dp} and d_{cp} were 5.5 mm, the system had the best heat dissipation performance. Next, in order to analyze the heat dissipation performance of Y-type BTMS when d_{dp} and d_{cp} are not equal, the sum of d_{dp} and d_{cp} was set to 11 mm, while the other dimensions and conditions remained unchanged. As shown in Figure 9,

d_{dp} increased from 4.5 mm to 8 mm, and the corresponding d_{cp} decreased from 6.5 mm to 3.0 mm. As d_{dp} increased, the heat dissipation performance of the system improved, with little change in the heat dissipation performance when d_{dp} was 7.0 mm, 7.5 mm and 8.0 mm. When d_{dp} and d_{cp} were 8.0 mm and 3.0 mm respectively, the system had the best heat dissipation performance, with T_{\max} of 40.269 °C and ΔT_{\max} of 0.392 °C.

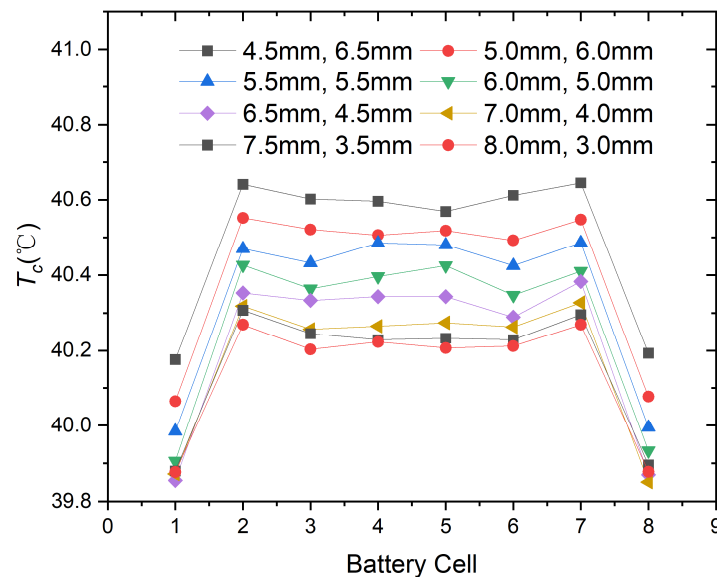


Figure 9. The heat dissipation performance of Y-type BTMS when d_{dp} and d_{cp} are not equal; the sum of d_{dp} and d_{cp} is set to 11 mm.

As shown in Figure 10, we analyzed the effect of d_{cp} on the system's heat dissipation performance when d_{dp} was kept at 8.0 mm. It was found that the system's heat dissipation performance improved with the decrease in d_{cp} . Considering the deployment of batteries, the minimum value of d_{cp} was set to 1.5 mm. When d_{cp} was 1.5 mm, T_{\max} was 40.06 °C and ΔT_{\max} was 0.266 °C.

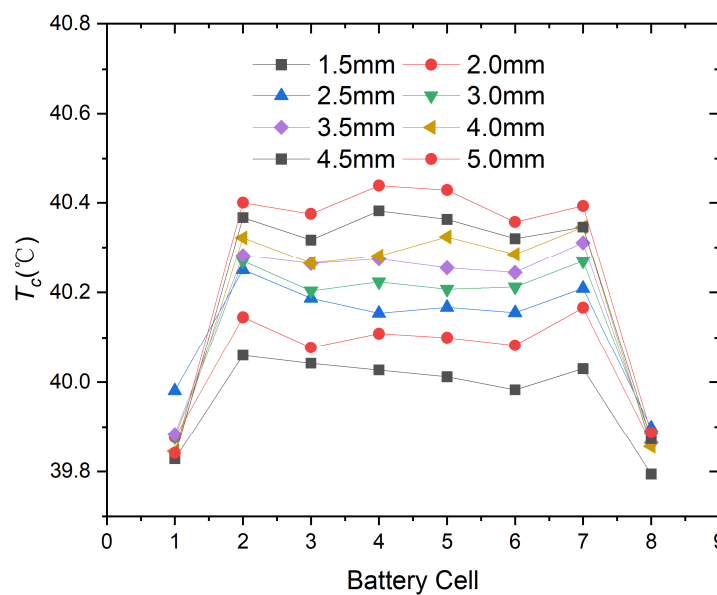


Figure 10. The system's heat dissipation performance when the d_{dp} was kept at 8.0 mm.

Figure 11 shows the air flow velocity in the X-axis cross-section (in channel 5), where d_{dp} is 8.0 mm. The dimensions of the cross-section on the Y-axis and Z-axis are the same as the projected dimensions of the battery cells on the Y-axis and Z-axis, allowing a better observation of the effect of flow velocity on heat dissipation performance. It can be clearly seen from Figure 11 that as d_{cp} decreases, V_{\max} increases.

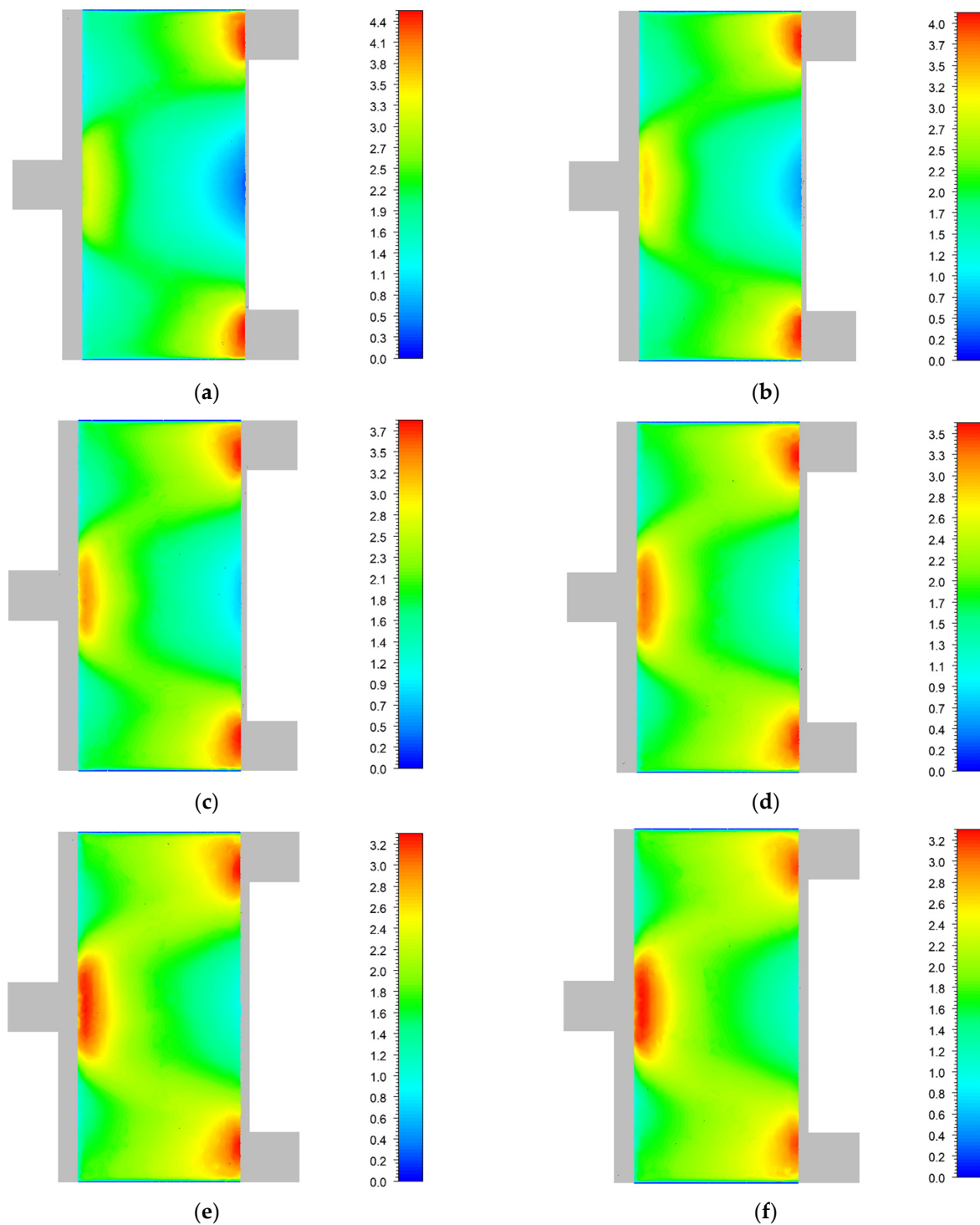


Figure 11. Cont.

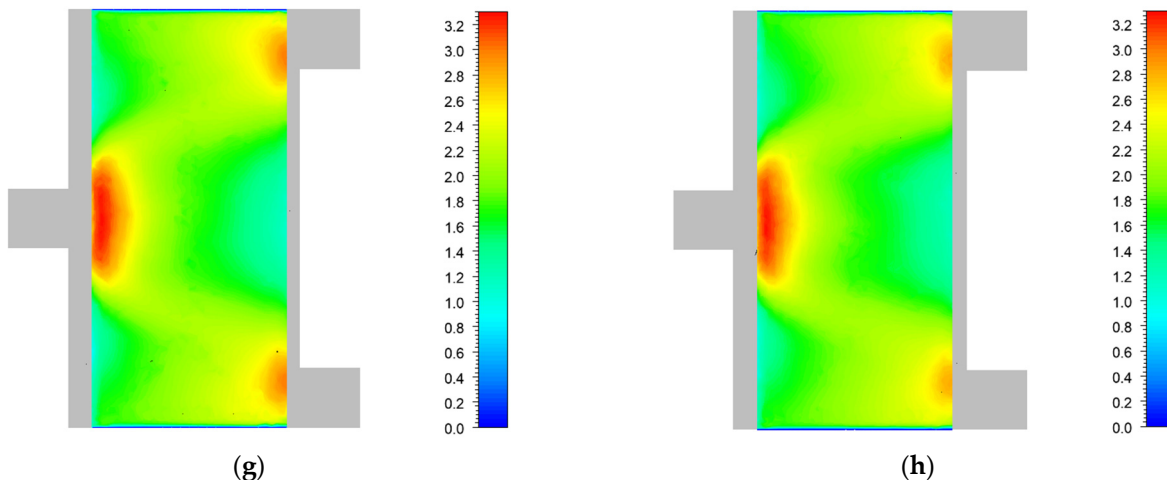


Figure 11. The air flow velocity in the X-axis cross-section, where d_{dp} is 8.0 mm. (a) $d_{cp} = 1.5$ mm; (b) $d_{cp} = 2.0$ mm; (c) $d_{cp} = 2.5$ mm; (d) $d_{cp} = 3.0$ mm; (e) $d_{cp} = 3.5$ mm; (f) $d_{cp} = 4.0$ mm; (g) $d_{cp} = 4.5$ mm; (h) $d_{cp} = 5.0$ mm.

As mentioned earlier, increasing air flow can better remove heat and improve system heat dissipation performance. From Figure 12, it can be seen that when d_{dp} was 8.0 mm, the effect of d_{cp} on T_{max} and V_{max} was significant. When d_{cp} decreased from 5.0 mm to 3.5 mm, V_{max} remained basically unchanged at approximately 3.300 m/s. When d_{cp} decrease from 3.5 mm to 1.5 mm, V_{max} rapidly increase from 3.336 m/s to 4.502 m/s, and correspondingly, T_{max} decreased from 40.311 °C to 40.06 °C.

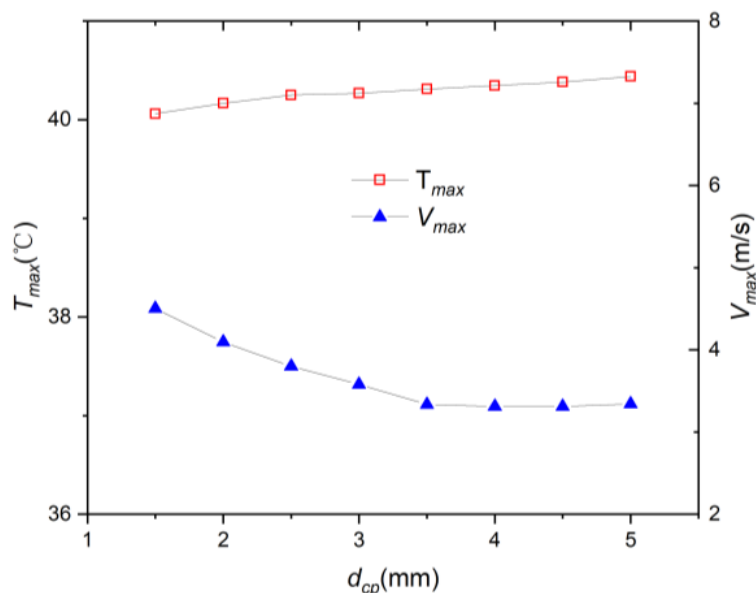


Figure 12. The effect of d_{cp} on T_{max} and V_{max} at the cross-section in the X-axis. d_{dp} is 8.0 mm.

3.2. Influence of Cooling Channel Width on Temperature Uniformity

From the temperature distribution of the eight batteries in the BTMS shown in Figure 10, it can be seen that the minimum value of T_c occurred on both sides of the battery pack, indicating that batteries 1 and 8 had the best heat dissipation effect. This is easy to understand because the air in cooling channels 1 and 9 only needed to take away the heat of one adjacent battery, while the air in other cooling channels needed to take away the heat of two adjacent batteries, as shown in Figure 5. Based on this, we

can improve temperature uniformity by adjusting the width of cooling channels 1 and 9, thereby reducing the flow rate of these two channels.

On the basis of the sample size in Figure 12, keeping d_{dp} and d_{cp} unchanged at 8.0 mm and 1.5 mm, respectively, we reduced d_1 and d_9 and made them equal, while keeping the width of the other cooling channels unchanged at 3 mm. The influence of d_1 and d_9 on the temperature of the battery pack is shown in Figure 13; the air flow velocity here was still 1.52 m/s. Due to the change in d_1 , the total flow rate was no longer $5.2 \times 10^{-3} \text{ m}^3 \cdot \text{s}^{-1}$. It can be seen that as d_1 decreased from 3.0 mm to 2.2 mm, the T_c value of the middle six battery cells gradually decreased, while the T_c value of the remaining batteries, numbers 1 and 8, did not change a great deal. As a result, the heat dissipation performance and temperature uniformity of the BTMS were improved. As d_1 continued to decrease from 2.2 mm, the T_c value of the middle six battery cells still gradually decreases, but the T_c value of battery cells 1 and 8 gradually increased and exceeded that of the middle six battery cells, resulting in a decrease in the temperature uniformity of the system. When d_1 was 2.2 mm, T_{\max} was 39.84 °C and ΔT_{\max} is 0.066 °C, the system had the best heat dissipation performance and temperature uniformity. T_{\max} and ΔT_{\max} of the best sample were 1.537 °C (3.68%) and 0.059 °C (47.2%) lower than those of the T-type model.

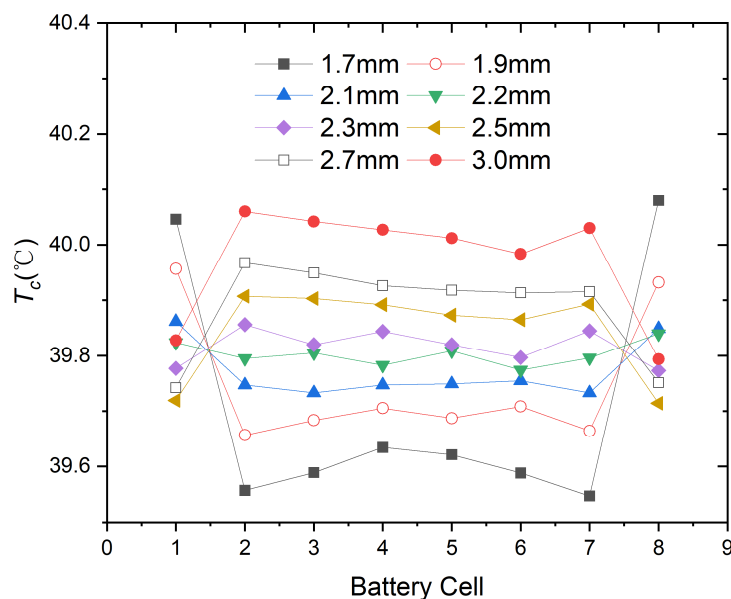


Figure 13. The influence of d_1 and d_9 on the temperature of the battery pack.

When d_1 changes, the improvement of system heat dissipation performance may be related to the changes in flow velocity in all cooling channels, while the improvement of system temperature uniformity may be related to the changes in flow velocity in cooling channels 1 and 9. Figure 14 shows the system flow velocity cloud map with changes in d_1 , with the cross-section taken from the middle section of the battery pack in the Y-axis direction. It can be seen that as d_1 decreased, there was indeed a significant change in the flow velocity of all channels and the flow velocity of cooling channels 1 and 9.

Figure 15 shows the maximum flow velocities of cooling channel 1 and all cooling channels when d_1 changed, with d_1 ranging from 1.7 mm to 3.0 mm. When d_1 decreased, the V_{\max} value of all cooling channels gradually increased from 2.432 m/s to 2.718 m/s. Therefore, the V_{\max} value of all cooling channels in Figure 13 can be used to explain the overall heat dissipation performance T_{\max} .

As shown Figure 15, when d_1 decreased from 3.0 mm to 2.5 mm, the V_{\max} value of cooling channel 1 gradually increased from 2.224 m/s to 2.300 m/s, corresponding to the T_c of battery cell 1 gradually decreasing from 39.828 °C to 39.719 °C in Figure 13. As shown in the same figure, when d_1 decreased from 2.5 mm to 1.7 mm, the V_{\max} of cooling channel

1 gradually decreased from 2.300 m/s to 2.064 m/s, corresponding to the T_c of battery cell 1 gradually increasing from 39.719 °C to 39.956 °C in Figure 13. Therefore, the V_{max} of cooling channel 1 can be used to explain the T_c of battery cell 1.

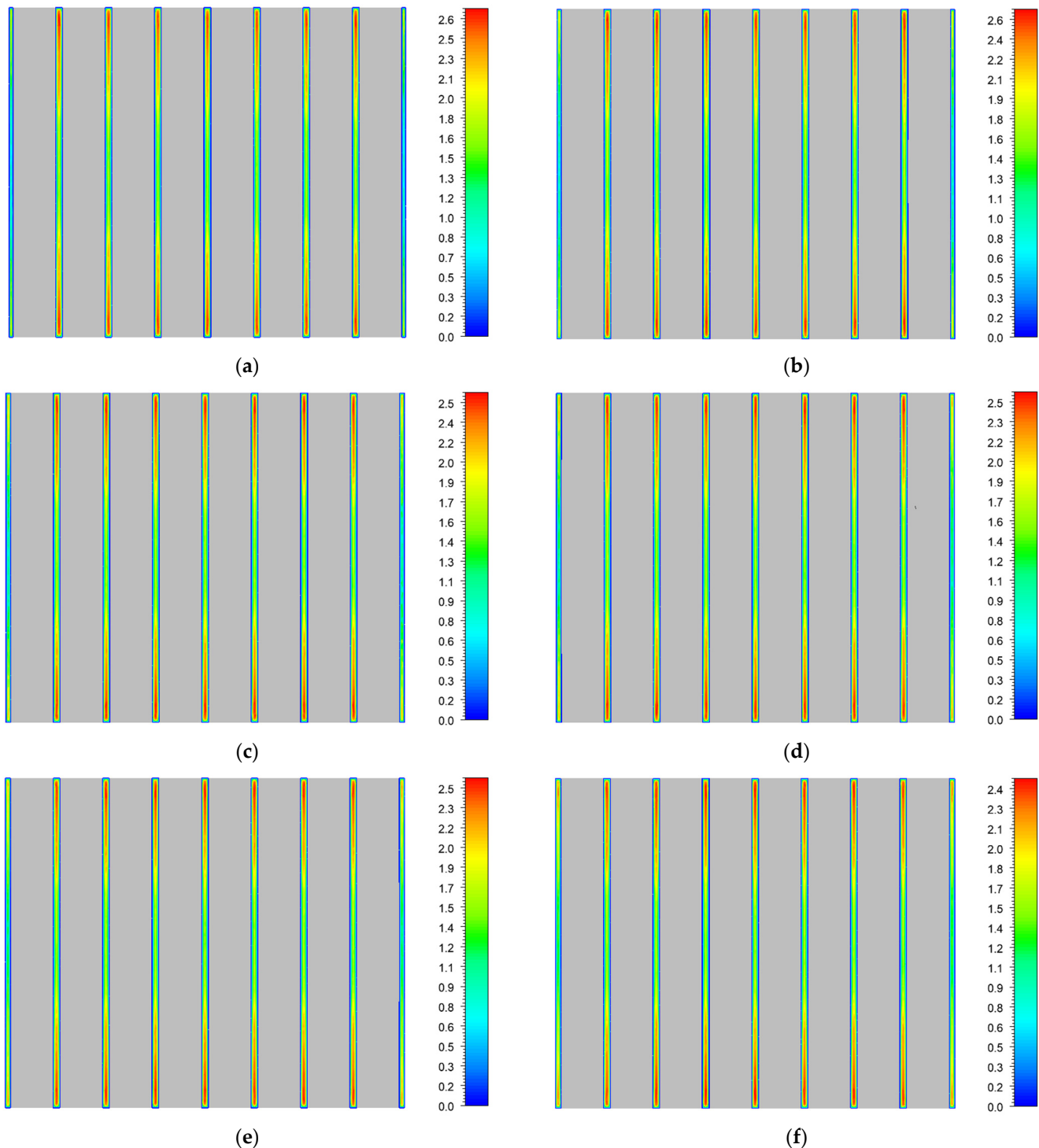


Figure 14. Cont.

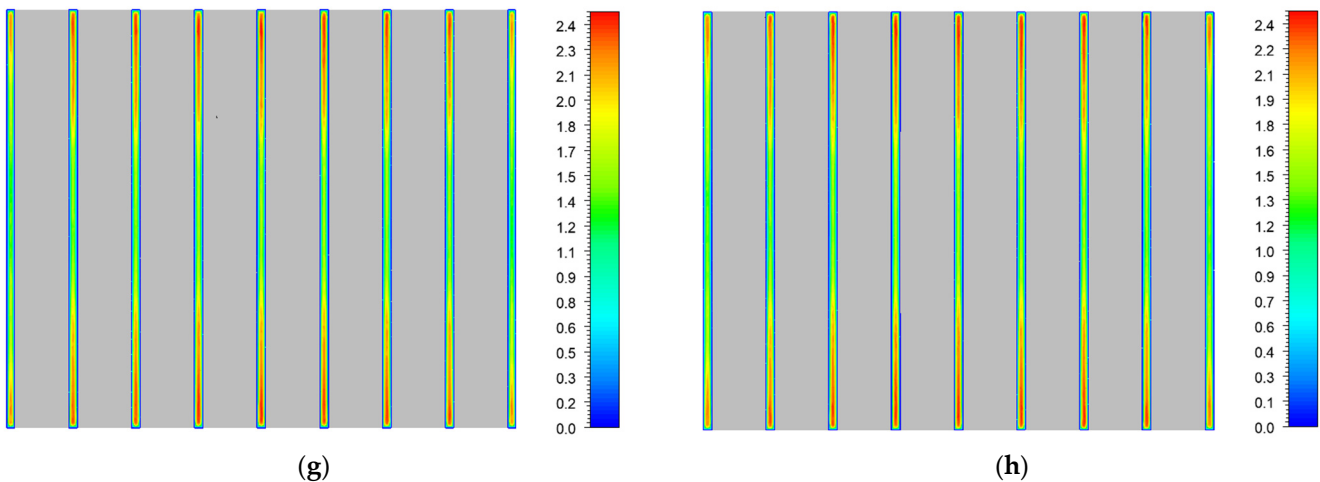


Figure 14. The system flow velocity cloud map with changes in d_1 and d_9 , with the cross-section taken from the middle section of the battery pack in the Y-axis direction. (a) $d_1 = d_9 = 1.7 \text{ mm}$; (b) $d_1 = d_9 = 1.9 \text{ mm}$; (c) $d_1 = d_9 = 2.1 \text{ mm}$; (d) $d_1 = d_9 = 2.2 \text{ mm}$; (e) $d_1 = d_9 = 2.3 \text{ mm}$; (f) $d_1 = d_9 = 2.5 \text{ mm}$; (g) $d_1 = d_9 = 2.7 \text{ mm}$; (h) $d_1 = d_9 = 3.0 \text{ mm}$.

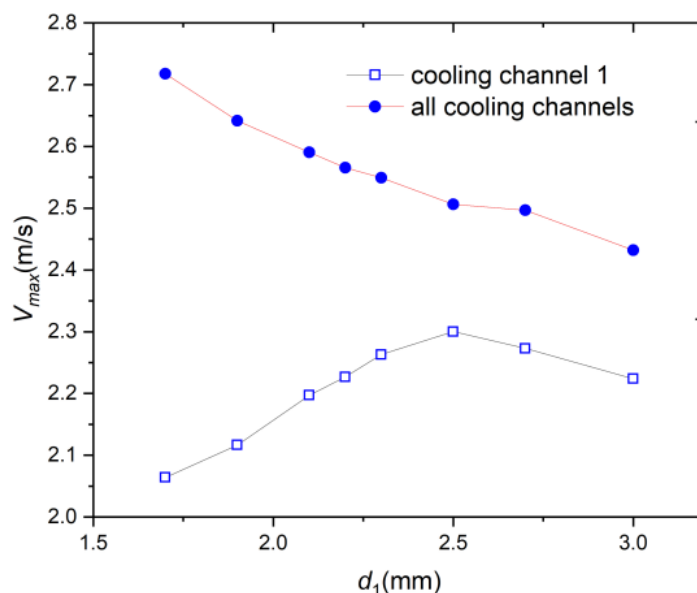


Figure 15. The maximum flow velocities of cooling channel 1 and all cooling channels when d_1 and d_9 change, with d_1 and d_9 ranging from 1.7 mm to 3.0 mm.

3.3. Inlet and Outlet

This study discusses the impact of d_{in} and d_{out} on system performance. Using the size of the best-performing sample in Figure 15, we kept d_{out} constant at 20 mm, and the impact of d_{in} on system performance is shown in Figure 16. When d_{in} increased from 12 mm to 26 mm, T_{max} and ΔT_{max} remained basically unchanged, with average values of 39.848°C and 0.074°C , respectively. Using the size of the best-performing sample shown in Figure 15, we once again kept d_{in} constant at 20 mm, and the effect of d_{out} on system performance is shown in Figure 17. When d_{out} increased from 12 mm to 26 mm, T_{max} and ΔT_{max} remained basically unchanged, with average values of 39.825°C and 0.055°C , respectively. Compared with the optimal results of the T-type BTMS with added turbulence in reference [5], the T_{max} and ΔT_{max} values of the T-type BTMS system were reduced by 1.537°C (3.71%) and 0.07°C (56%), respectively. It was observed that the T_{max} value of the

system was below 40 °C, and the battery cells were in the optimal operating temperature range of 20–40 °C.

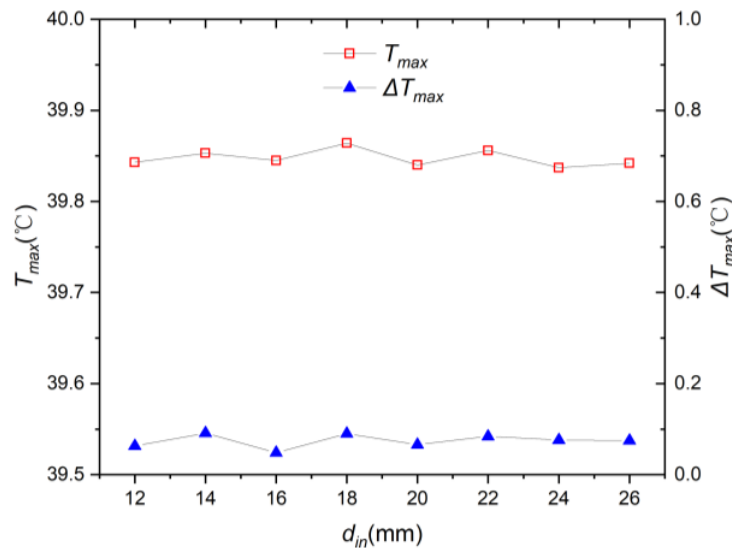


Figure 16. The impact of d_{in} on system performance.

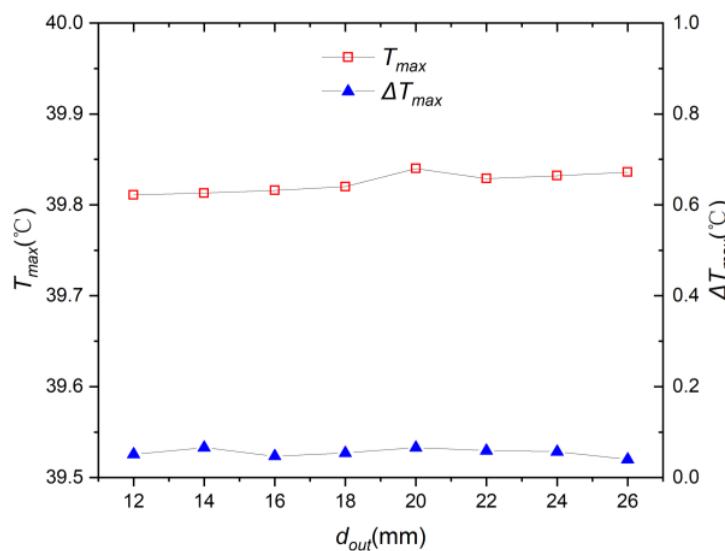


Figure 17. The effect of d_{out} on system performance.

3.4. Energy Consumption and Safety Analysis

3.4.1. Energy Consumption

When designing a BTMS, energy consumption needs to be considered [14,17]. For the purpose of quantitative evaluation, system energy consumption (W_p) is introduced to represent the energy consumed by BTMS, and the calculation formula is:

$$W_p = \Delta P_{in-out} \cdot Q_{in} \quad (9)$$

where ΔP_{in-out} is the pressure drop of the area-weighted average between the inlet and outlet, while Q_{in} is the inlet airflow rate.

The cooling performance and energy consumption of the BTMS at each design stage at the end of discharge at a 2.5 C discharge rate is summarized in Table 3, but the impacts of d_{in} and d_{out} are longer included. In the first three design stages, Q_{in} were $5.2 \times 10^{-3} \text{ m}^3 \cdot \text{s}^{-1}$.

In design stage 4, as mentioned earlier, due to the decrease in d_1 , Q_{in} was slightly lower than $5.2 \times 10^{-3} \text{ m}^3 \cdot \text{s}^{-1}$. The pressure at the outlet was close to zero; therefore, the system energy consumption was directly proportional to the inlet pressure.

Table 3. Cooling performance and energy consumption.

Stage	Factors		Results		
1	$d_{dp} = d_{cp}$ (mm)		T_{\max} (°C)	ΔT_{\max} (°C)	W_p (W)
	2.5		41.231	0.266	0.0942
	3.0		40.854	0.281	0.0766
	5.0		40.492	0.51	0.0458
	5.5		40.486	0.501	0.0425
	6.0		40.515	0.551	0.0396
	7.0		40.558	0.555	0.0355
	10.0		40.829	0.619	0.0299
	20.0		41.048	0.380	0.0258
2	d_{dp} (mm)	d_{cp} (mm)	T_{\max} (°C)	ΔT_{\max} (°C)	W_p (W)
	4.5	6.5	40.645	0.469	0.0447
	5.0	6.0	40.552	0.487	0.0432
	5.5	5.5	40.486	0.501	0.0425
	6.0	5.0	40.426	0.52	0.0422
	6.5	4.5	40.383	0.528	0.0423
	7.0	4.0	40.327	0.476	0.0441
	7.5	3.5	40.307	0.427	0.0464
	8.0	3.0	40.269	0.392	0.0501
3	$d_{dp} = 8 \text{ mm}$	d_{cp} (mm)	T_{\max} (°C)	ΔT_{\max} (°C)	W_p (W)
		1.5	40.06	0.266	0.0768
		2.0	40.166	0.302	0.0647
		2.5	40.25	0.352	0.0563
		3.0	40.269	0.392	0.0501
		3.5	40.311	0.447	0.0457
		4.0	40.346	0.501	0.0426
		4.5	40.382	0.549	0.0400
		5.0	40.438	0.597	0.0383
4	$d_{dp} = 8 \text{ mm}$, $d_{cp} = 1.5 \text{ mm}$	$d_1 = d_9$ (mm)	T_{\max} (°C)	ΔT_{\max} (°C)	W_p (W)
		1.7	40.08	0.533	0.0866
		1.9	39.956	0.3	0.0844
		2.1	39.862	0.129	0.0831
		2.2	39.84	0.066	0.0825
		2.3	39.856	0.083	0.0805
		2.5	39.907	0.193	0.0800
		2.7	39.967	0.225	0.0788
		3.0	40.06	0.266	0.0768

In design stage 1, when d_{dp} and d_{cp} increased simultaneously, energy consumption rapidly decreased. In design phase 2, when the sum of d_{dp} and d_{cp} remained constant, there was little change in energy consumption. In design phase 3, when d_{dp} remained constant and d_{cp} increased, energy consumption rapidly decreased. The results indicate that the reduction in energy consumption (pressure drop) is mainly influenced by d_{cp} . This suggests that we can reduce system energy consumption by increasing d_{cp} . Furthermore, from the results of the above three stages, it can be seen that the cooling performance of the system often deteriorates when power consumption decreases. When designing the BTMS structure, we need to seek a balance between cooling performance and energy consumption according to our needs. In design phase 4, we found that the energy consumption was less affected by d_1 . The energy consumption of sample with the best cooling performance was 0.0825 W, which was 0.0124 W (13.1%) lower than that of the T-type model.

3.4.2. Safety Analysis

The safety of batteries under extreme conditions is also crucial, such as BTMS being exposed to higher ambient temperatures and higher discharge rates. The sample with the best performance in stage 4 was selected for analysis, where d_1 was 2.2 mm. The performance of the BTMS is summarized in Table 4 for ambient temperatures of 25, 30 and 35 °C and discharge rates of 2.5, 3 and 4 C, respectively. When the ambient temperature was 35 °C and the discharge rate was 2.5 C, the T_{\max} value of BTMS at the end of discharge was below 50 °C, indicating good heat dissipation performance. ΔT_{\max} was very small under different conditions, indicating that the Y-type BTMS had excellent temperature uniformity. We found an interesting phenomenon from the results: while keeping the discharge rate constant, the relationship between T_{\max} and different ambient temperatures can be obtained. We hope to continue analyzing whether the pattern is universal in future research. The formula is as follows:

$$T_{\max,Ti} = T_{\max,Tj} + T_i - T_j \quad (10)$$

where T_i and T_j are two different ambient temperatures, while $T_{\max,Ti}$ and $T_{\max,Tj}$ are the maximum temperatures of the BTMS at ambient temperatures T_i and T_j , respectively.

Table 4. Safety analysis.

Ambient Temperature (°C)	Discharge Rate (C)	Results		
		T_{\max} (°C)	ΔT_{\max} (°C)	W_p (W)
25	2.5	39.84	0.066	0.0833
25	3	42.967	0.067	0.0833
25	4	49.077	0.064	0.0833
30	2.5	44.84	0.066	0.0833
30	3	47.967	0.067	0.0833
30	4	54.077	0.064	0.0833
35	2.5	49.84	0.066	0.0833
35	3	52.967	0.067	0.0833
35	4	59.077	0.064	0.0833

Finally, we studied the dynamic performance of battery heat dissipation in the BTMS. For an ambient temperature of 25 °C, the T_c of battery cell 4 of the sample in Table 4 at different discharge rates is shown in Figure 18; the other cells are almost the same. From Figure 4, it can be observed that the battery cell heated up rapidly in the initial stage and then gradually slowed down.

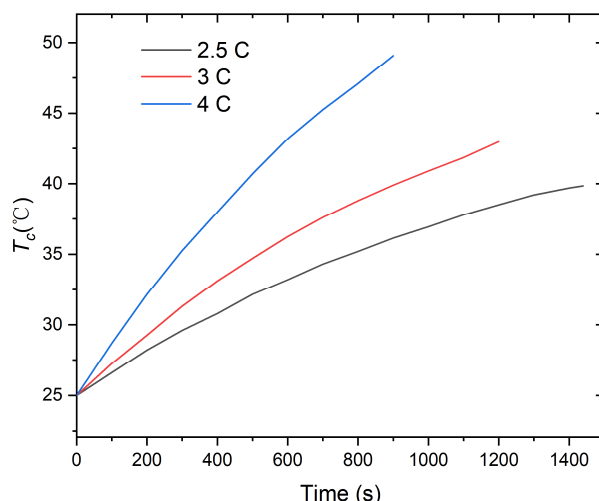


Figure 18. T_c of battery cell 4 at different discharge rates. The ambient temperature is 25 °C.

4. Conclusions

This paper proposes a Y-type air-cooled BTMS system with shortened airflow path characteristics. Several important conclusions of the study are as follows:

- (1) By adjusting the depths of the distribution plenum and convergence plenum, the airflow velocities passing through the vicinities of the battery cells can be changed, thereby reducing T_{\max} . When d_{dp} remains at 8.0 mm and d_{cp} decreases from 3.5 mm to 1.5 mm, V_{\max} rapidly increases, and the corresponding T_{\max} can be reduced to 40.06 °C.
- (2) By changing the width of cooling channels 1 and 9, the flow velocity of these two channels can be adjusted to improve the temperature uniformity of the system. When d_1 and d_9 decrease from 3.0 mm to 1.7 mm, the T_c value of the middle six batteries gradually decreases, and the T_c value of batteries 1 and 8 first decreases and then increases. When d_1 and d_9 are 2.2 mm, the heat dissipation performance and temperature uniformity of the system are optimal, with T_{\max} of 39.84 °C and ΔT_{\max} of 0.066 °C. The maximum flow velocity of all cooling channels and the maximum flow velocity of cooling channel 1 can be used separately to analyze T_{\max} and T_c of battery cell 1.
- (3) The inlet and outlet widths have little effect on the heat dissipation performance and temperature uniformity of the system. When d_{out} increases from 12 mm to 26 mm, the average values of the T_{\max} and ΔT_{\max} are 39.825 °C and 0.055 °C, respectively. The battery cells in the system are still within the optimal operating temperature range of 20–40 °C. ΔT_{\max} is less than 0.1 °C, and the system achieves excellent temperature uniformity.
- (4) The cooling performance and energy consumption of the BTMS at each design stage at the end of a 2.5 C discharge rate are summarized. The results indicate that the reduction in energy consumption (pressure drop) is mainly influenced by d_{cp} . The energy consumption of the sample with the best cooling performance is 0.0825 W, which is 0.0124 W (13.1%) lower than that of the T-type model.
- (5) ΔT_{\max} is very small when the BTMS is exposed to higher ambient temperatures and higher discharge rates, indicating that the BTMS has excellent temperature uniformity. Keeping the discharge rate constant, the relationship between T_{\max} and different ambient temperatures can be obtained.

Author Contributions: Conceptualization, J.L.; methodology, J.L.; software, J.L.; validation, X.L. (Xiangyang Li), J.L. and X.L. (Xiaomin Li); formal analysis, X.L. (Xiaomin Li); investigation, X.L. (Xiaomin Li); resources, X.L. (Xiaomin Li); data curation, X.L. (Xiangyang Li); writing—original draft preparation, X.L. (Xiangyang Li); writing—review and editing, X.L. (Xiangyang Li); visualization, X.L. (Xiaomin Li); supervision, J.L.; project administration, J.L.; funding acquisition, X.L. (Xiangyang Li), J.L. and X.L. (Xiaomin Li). All authors have read and agreed to the published version of the manuscript.

Funding: This work was supported by the Huzhou Natural Science Foundation (Nos. 2022YZ43 and 2022YZ01), the Henan Province Science and Technology Key Project under Grant No. 232102211071, and the Project for Huzhou Key Laboratory of IoT Intelligent System Integration Technology under Grant No. 2022-21.

Data Availability Statement: The data are contained within the article.

Conflicts of Interest: The authors declare no conflicts of interest.

References

1. Gibbons, L.; Javed, S. A review of HVAC solution-sets and energy performance of nearly zero-energy multi-story apartment buildings in Nordic climates by statistical analysis of environmental performance certificates and literature review. *Energy* **2022**, *238*, 121709. [CrossRef]
2. Asif, A.; Abdul, R.R.K.; Mohammed, S.A.D.; Rahul, K.; Mit, A.; Goon, P.S. A critical review on renewable battery thermal management system using heat pipes. *J. Therm. Anal. Calorim.* **2023**, *16*, 148.

3. Hajidavalloo, M.R.; Chen, J.; Hu, Q.; Song, Z.; Yin, X.; Li, Z. NMPC-Based integrated thermal management of battery and cabin for electric vehicles in cold weather conditions. *IEEE Trans. Intell. Veh.* **2023**, *8*, 4208–4222. [[CrossRef](#)]
4. Kiani, M.; Omiddezyani, S.; Houshfar, E.; Miremadi, S.R.; Ashjaee, M.; Nejad, A.M. Lithium-ion battery thermal management system with Al₂O₃/AgO/CuO nanofluids and phase change material. *Appl. Therm. Eng.* **2020**, *180*, 115840. [[CrossRef](#)]
5. Shen, K.; Yang, L.; Sun, J.; Xu, C.; Wang, H.; Zheng, Y.; Feng, X. Experimental and simulations study of thermal performance of cell-to-pack structure for a lithium-ion battery pack. *J. Electrochem. Energy Convers. Storage* **2023**, *20*, 041003. [[CrossRef](#)]
6. Zhao, C.; Cao, W.; Dong, T.; Jiang, F. Thermal behavior study of discharging/charging cylindrical lithium-ion battery module cooled by channeled liquid flow. *Int. J. Heat Mass Transf.* **2018**, *120*, 751–762. [[CrossRef](#)]
7. Ravikumar, B.; Mynam, M.; Rai, B. Molecular dynamics investigation of electric field altered behavior of lithium ion battery electrolytes. *J. Mol. Liq.* **2020**, *300*, 112252. [[CrossRef](#)]
8. Lu, Z.; Yu, X.; Wei, L.; Qiu, Y.; Zhang, L.; Meng, X.; Jin, L. Parametric study of forced air cooling strategy for lithium-ion battery pack with staggered arrangement. *Appl. Therm. Eng.* **2018**, *136*, 28–40. [[CrossRef](#)]
9. Wang, T.; Tseng, K.J.; Zhao, J. Development of efficient air-cooling strategies for lithium-ion battery module based on empirical heat source model. *Appl. Therm. Eng.* **2015**, *90*, 521–529. [[CrossRef](#)]
10. Hong, S.; Zhang, X.; Chen, K. Design of flow configuration for parallel air-cooled battery thermal management system with secondary vent. *Int. J. Heat Mass Transf.* **2018**, *116*, 1204–1212. [[CrossRef](#)]
11. Yu, K.; Yang, X.; Cheng, Y.; Li, C. Thermal analysis and two-directional air flow thermal management for lithium-ion battery pack. *J. Power Sources* **2014**, *270*, 193–200. [[CrossRef](#)]
12. Shahid, S.; Agelin-Chaab, M. Development and analysis of a technique to improve air-cooling and temperature uniformity in a battery pack for cylindrical batteries. *Therm. Sci. Eng. Prog.* **2018**, *5*, 351–363. [[CrossRef](#)]
13. Peng, X.; Ma, C.; Garg, A.; Bao, N.; Liao, X. Thermal performance investigation of an aircooled lithium-ion battery pack considering the inconsistency of battery cells. *Appl. Therm. Eng.* **2019**, *153*, 596–603. [[CrossRef](#)]
14. Zhang, F.; Yi, M.; Wang, P.; Liu, C. Optimization design for improving thermal performance of T-type air-cooled lithium-ion battery pack. *J. Energy Storage* **2021**, *44*, 103464. [[CrossRef](#)]
15. Chen, K.; Song, M.; Wei, W.; Wang, S. Design of the structure of battery pack in parallel air-cooled battery thermal management system for cooling efficiency improvement. *Int. J. Heat Mass Transf.* **2019**, *132*, 309–321. [[CrossRef](#)]
16. Zhang, F.; Lin, A.; Wang, P.; Liu, P. Optimization design of a parallel air-cooled battery thermal management system with spoilers. *Appl. Therm. Eng.* **2021**, *182*, 116062. [[CrossRef](#)]
17. Weng, J.; Xiao, C.; Yang, X.; Ouyang, D.; Chen, M.; Zhang, G.; Waiming, L.E.; Yuen, K.K.R.; Wang, J. An energy-saving battery thermal management strategy coupling tubular phase-change-material with dynamic liquid cooling under different ambient temperatures. *Renew. Energy* **2022**, *195*, 918–930. [[CrossRef](#)]

Disclaimer/Publisher's Note: The statements, opinions and data contained in all publications are solely those of the individual author(s) and contributor(s) and not of MDPI and/or the editor(s). MDPI and/or the editor(s) disclaim responsibility for any injury to people or property resulting from any ideas, methods, instructions or products referred to in the content.